POLITECNICO DI TORINO
Repository ISTITUZIONALE

A time-saving and cost-effective method to process alloys by Laser Powder Bed Fusion

*Original*
A time-saving and cost-effective method to process alloys by Laser Powder Bed Fusion / Bosio, F., Aversa, A., Lorusso, M., Marola, S., Gianoglio, D., Battezzati, L., Fino, P., Manfredi, D., Lombardi, M.. - In: MATERIALS & DESIGN. - ISSN 0264-1275. - ELETTRONICO. - 181:107949(2019). [10.1016/j.matdes.2019.107949]

*Availability:*
This version is available at: 11583/2740972 since: 2019-07-10T04:17:56Z

*Publisher:*
Elsevier Ltd

*Published*
DOI:10.1016/j.matdes.2019.107949

*Terms of use:*

This article is made available under terms and conditions as specified in the corresponding bibliographic description in the repository

*Publisher copyright*

(Article begins on next page)

09 October 2026

Materials and Design 181 (2019) 107949

Contents lists available at ScienceDirect

Materials and Design

journal homepage: www.elsevier.com/locate/matdes

# A time-saving and cost-effective method to process alloys by Laser Powder Bed Fusion

Federico Bosio [a,*], Alberta Aversa [a], Massimo Lorusso [b], Silvia Marola [c], Dario Gianoglio [c], Livio Battezzati [c], Paolo Fino [a], Diego Manfredi [b], Mariangela Lombardi [a]

[a] Department of Applied Science and Technology, Politecnico di Torino, Corso Duca degli Abruzzi 24, 10129 Torino, Italy
[b] Center for Sustainable Future Technologies CSFT@Polito, Istituto Italiano di Tecnologia, Via Livorno 60, 10144 Torino, Italy
[c] Dipartimento di Chimica, Università di Torino, Torino, Italy

## HIGHLIGHTS

- A time- and cost-effective method to manufacture new alloys by Laser Powder Bed Fusion (LPBF) is proposed.
- Definition of main process parameters for processing new alloys for LPBF is achieved by means of Single Scan Tracks (SSTs).
- A proper overlap between nearby SSTs is the key for defining the proper hatching distance for high density massive samples.
- A scenario of hardness and productivity vs. energy density is given for a new Al alloy: AlSi10Mg + 4 wt% Cu mixed alloy.

## GRAPHICAL ABSTRACT

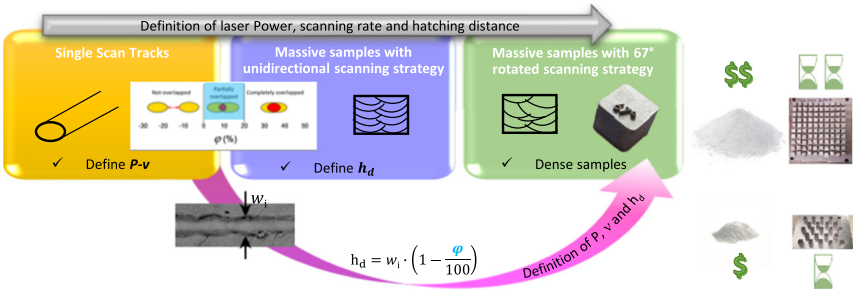


## ARTICLE INFO

*Article history:*
Received 25 March 2019
Received in revised form 1 June 2019
Accepted 14 June 2019
Available online 16 June 2019

*Keywords:*
Laser Powder Bed Fusion (LPBF)
Single scan tracks (SSTs)
Hatching distance ($h_d$)
Overlap
Process parameters
Hardness
Build-up rate

## ABSTRACT

Definition of the main process parameters, laser power ($P$), scanning speed ($v$), hatching distance ($h_d$) and scanning strategy useful for producing dense samples, is fundamental to develop novel alloy compositions for Laser Powder Bed Fusion (LPBF). The present work has two aims: on one side, to verify the processability of a new AlSi10Mg + 4Cu alloy of mixed powders by LBPF; on the other side, on the basis of the experimental analysis, to define a method for processing new alloys. Producing Single Scan Tracks (SSTs), samples with unidirectional scanning strategy and samples with 67° rotated scanning strategy, the proper $P$-$v$-$h_d$ combinations were identified reaching a final porosity lower than 1.5%. A scenario of hardness and build-up rate vs. energy density is given, to adopt the main process parameters suitable to maximize mechanical properties or productivity. According to the novel method, $P$-$v$-$h_d$ combinations can be defined through the production and characterization of SSTs and samples with 67° rotated scanning strategy. Through two production steps dense samples can be then obtained, allowing the development of new compositions saving time and reducing costs related to the powder usage.

© 2019 The Authors. Published by Elsevier Ltd. This is an open access article under the CC BY license (http://creativecommons.org/licenses/by/4.0/).

## 1. Introduction

Additive manufacturing (AM) of metal parts is widely recognized as a powerful alternative to conventional casting routes for medium-low batch productions, thanks to its capability to manufacture complex shaped parts with high design freedom and without the needs for

* Corresponding author at: Politecnico di Torino, Corso Duca degli Abruzzi 24, 10129 Torino, Italy.
*E-mail address:* federico.bosio@polito.it (F. Bosio).

https://doi.org/10.1016/j.matdes.2019.107949
0264-1275/© 2019 The Authors. Published by Elsevier Ltd. This is an open access article under the CC BY license (http://creativecommons.org/licenses/by/4.0/).

further assembling or post-process joining [1]. AM is considered a strategic technology and a key enabler for accelerated engineering processes. Moreover, metallic AM opens completely new opportunities to design novel alloy compositions with specific properties which cannot be generated in conventional processes, due to its peculiar conditions, similar to those of rapid solidification processes [2]. Laser Powder Bed Fusion (LPBF) has been the AM technique used most extensively during the last decade [3]. This process is also known as Selective Laser Melting (SLM), but now the term SLM is associated with the use of a specific commercial machine (SLM Solutions, Germany). Nowadays, there are only a limited number of alloy systems available in the marketplace for LPBF, the most widespread being pure titanium and Ti6Al4V alloy, stainless steels, nickel-based superalloys, Al-Si—casting alloys, cobalt chromium and recently high-entropy alloys [4–11]. Therefore, to exploit all the benefits of LPBF, developing new alloy compositions of industrial interest is now becoming a key challenge to address in the field [12]. However, the development of new alloys for LPBF is not a simple route and, generally, it requires high economical investments. As an example, the high cost of the starting powder significantly increases the price of final parts: powder costs are the second largest cost associated with producing LPBF parts [13]. In fact, as a rule for all powder bed systems, highly spherical gas-atomized powders with specific particle size distribution are required to guarantee good flowability and to prevent the formation of porosities [14,15]. Since few companies are able to gas-atomize such powders, whenever a novel metal system is investigated, an ad-hoc customized powder can be rather expensive and quite difficult to purchase on the market in a short time. Once a suitable powder is produced, finding the right window for the main process parameters is a core procedure for adopting novel alloy compositions for LPBF. In this respect, the main goal is to reach the highest level of density, near the theoretical one. There are many process parameters that can affect layer by layer adhesion with direct influence on the final density of the parts. Considering a fixed value for the layer thickness, selected on the basis of the powder mean size and distribution, the main process parameters are laser power ($P$), scan speed ($v$), hatching distance ($h_d$) and scanning strategy [16]. Recent findings in literature demonstrate that the proper $P$ and $v$ values for LPBF of an alloy can be determined via the Single Scan Tracks (SSTs) approach, which requires very small quantity of powders with respect to the manufacturing of massive samples [9,17–22]. In fact, an SST corresponds to a laser track made by the effective laser spot diameter on a single powder layer previously spread onto a substrate. In LPBF the quality of the 3D manufactured object strongly depends on the quality of each single track. For this reason, many experimental analyses on the formation and behaviour of single laser tracks have been extensively carried out to evaluate the melting and consolidation behaviour of the material. For example, considering Ni-based superalloys, Li et al. identified a good operating window of Inconel 625 according to SSTs characteristics [19]. They observed that defects and porosity were more prone to form in tracks built at high laser power due to the turbulence of the melt pool, the melt pool being the cross-section of a single laser scan track. Considering Al alloys, Kempen et al. observed that the highest densities of AlSi10Mg parts produced by SLM were reached when the Linear Energy Density (LED) was optimal to produce regular tracks with stable melt pools [9]. In agreement with this, in a recent study, Wei et al. showed that the large amount of pores in SLM*ed* AlSi10Mg samples built with a parameter combination corresponding to a low LED were mainly caused by the discontinuous scan tracks used in the manufacturing [20]. However, in view of the production of 3D components, to determine the process window it is also fundamental to consider the effect of the other main process parameters, i.e. the $h_d$ and the scanning strategy. In particular, the hatching distance is the distance between consecutive and adjacent laser scan tracks on each layer, forming shapes like stripes or square islands of different size to melt the powder in correspondence to the section of the 3D component [16]. The scanning strategy is related to the path followed by the laser to fill the section in each layer: these in-layer patterns can be created unidirectionally, along horizontal (x-axis) or vertical (y-axis) directions, both in x and y or alternating in x and y, inclined at various angles (45°, 67° or 90°) across successive layers [23]. To determine the operating window, massive samples, like cubes or parallelepipeds, are directly produced and traditional Design Of Experiment (DOE) approaches, such as full factorial design [24], two-level fractional factorial design [25] and response surface method [26], are widely used. Despite the successful results that can be obtained using these approaches, the production of a great number of specimens and time-intensive experiments are required [24–27]. Hence, considering the high usage of powder and the working time for samples production, this approach also means high costs.

Recently, Nie et al. studied the effect of processing parameters on the formation of single scan track, multi tracks and cubic samples for a SLMed Al-Cu-Mg gas-atomized powder [22]. For the specific alloy selected for their work, the Authors experimentally determined $P$ and $v$ values starting from SSTs analysis. After that, they produced multi tracks to determine $h_d$ through the surface roughness evaluation. Finally, they produced dense samples, adopting a fixed value of layer thickness and a 90° rotated scanning strategy, characterizing them in terms of microstructure and hardness. Their experimental study highlights the importance of a proper overlap between nearby single tracks.

Starting from the work of Nie et al., in the present study the LPBF processability of a new Al alloy with a customized composition is investigated by realizing SSTs, massive samples with unidirectional scanning strategy and finally massive samples with rotated scanning strategy by using mixed AlSi10Mg + 4Cu powder, cheaper than gas-atomized ones. The first jobs allowed us to select a range of $P$-$v$ values for which stable and regular SSTs were obtained. After that, massive samples were built with unidirectional scanning strategy to identify the proper $h_d$ for reducing residual porosity. Finally, massive samples produced with a 67° rotated scanning strategy gave information about the mechanical performances of LPBF materials and of their production rates. On the basis of these results, a time- and cost-effective innovative method to manufacture new alloys for LPBF is defined. According to the proposed methodology, SSTs are performed identifying the continuous and stable ones, controlled by $P$ and $v$. At this point the measurement of SST width allows to directly select the $h_d$ value to ensure a good overlapping and, therefore, the direct manufacturing of dense samples with rotated scanning strategy.

## 2. Materials and methods

### 2.1. Raw material

Pre-alloyed gas-atomized powder of AlSi10Mg and high purity Cu (HCP Cu) powder, supplied respectively by EOS Gmbh and Sandvik Osprey LTD, were mixed for 24 h at a speed of 60 rpm by using ceramic jars without grinding media. This mixing technique was adopted in order to avoid the deformation of the starting powder and preserve its flowability. The chemical composition of the starting powders together with the calculated AlSi10Mg + 4Cu alloy composition are summarized in Table 1. The mixed powder was firstly investigated by means of a Field Emission Scanning Electron Microscope (FESEM) Zeiss SupraTM 40 to estimate particle morphology and, then, by using a laser

**Table 1**
Chemical composition of the used powder (wt%) as declared by the suppliers; *the mixed one is calculated starting from the previous two compositions.

| Alloy | Si | Fe | Cu | Mn | Mg | Ti | O | Al |
|---|---|---|---|---|---|---|---|---|
| AlSi10Mg | 9–11 | ≤0.55 | ≤0.05 | ≤0.45 | 0.2–0.45 | ≤0.15 | – | Bal. |
| HCP Cu | – | – | ≥99.96 | – | – | – | ≤0.04 | – |
| AlSi10Mg + 4Cu* | 8.6–10.6 | ≤ 0.55 | 4 | ≤0.45 | 0.19–0.43 | ≤0.15 | ≤0.04 | Bal. |

granulometer Fritsch Analysette 22 Compact to determine the size distribution, adopting a volumetric assumption. As shown in Fig. 1a the mixed powder consists of mostly spherical particles indicating that the mixing has not damaged the starting particles. A consistent fraction of fine particles of a size below 5 μm tend to adhere to the coarsest ones resulting in the formation of large clusters of about 20–30 μm. Some Cu particles with varied sizes can be clearly observed among AlSi10Mg particles, indicated by white arrows in Fig. 1a. Particle diameters corresponding to 10% ($d_{10}$), 50% ($d_{50}$) and 90% ($d_{90}$) of the cumulative size distribution are 13.3, 28.2 and 44.8 μm, respectively (Fig. 1b). Considering these results and previous studies on aluminium alloys [16,21], a value of 30 μm for the layer thickness during the process was fixed.

### 2.2. Single Scan Tracks (SSTs) preparation and characterization

SSTs of AlSi10Mg + 4Cu mixed alloy were built by an EOSINT M270 Dual mode system (EOS Gmbh). In this system, a Yb-fiber laser is used to locally melt a thin powder layer with a wavelength of 1070 nm, a continuous power up to 200 W, a spot of 100 μm and a scanning speed up to 7000 mm/s. The building chamber provides a closed environment filled by argon as a protective gas. To reduce the thermal stresses between substrate and deposited tracks, the building platform was preheated at 100 °C. A modified building platform with removable discs of cast AlSi10Mg and of 40 mm diameter was adopted in the production of SSTs according to the system proposed by Aversa et al. [21]. The chemical composition of the disc was intentionally chosen as close as possible to the deposited alloy in order to prevent any contamination in the molten pool composition after the laser melting. To prepare the SSTs, a single powder layer of 50 μm thickness was accurately deposited using a self-developed recoating system only on the discs. This value was selected considering the real layer thickness obtained using a 30 μm as building platform displacement. The length of each scan track was 9 mm for all the experiments.

Two set of SSTs were built in two jobs with the process parameters summarized in Table 2. A 5 × 5 matrix of $P \times v$ for a total of 25 combinations was used for the first job. On the basis of an Authors previous work related to SST analysis of Al alloys [21], for the first, preliminary investigation wide $P$ - $v$ ranges were chosen. In particular, for the purpose of quickly verifying the processability of AlSi10Mg + 4Cu alloy, the region for stable and regular tracks of AlSi10Mg was considered. The produced SSTs were characterized through on-top analysis by means of an optical microscope (OM) LEICA DMI 5000 M. Then, samples for melt pool characterization of SSTs were cut from the discs using a diamond saw, mounted in a thermosetting resin, polished by standard metallographic technique up to 1 μm and finally observed by OM. Melt pool sections were taken in the middle of the scan track to ensure a reliable shape not affected by border instabilities [28]. The geometrical features of the investigated melt pool, i.e. width ($w$), total height ($h$), growth ($g$) and penetration in the substrate ($d$) as schematized in Fig. A1, were evaluated by post-processing the corresponding melt pool micrographs via image analysis software ImageJ. Two main melt pool shape indicators were derived from this analysis: the total height to width ratio ($h/w$) and the growth to depth ratio ($g/d$). In order to fine tune the $P$-$v$ range, in the second SST job a narrow 3 × 4 matrix with regular intervals of 10 W and 100 mm/s were adopted in the region of stable and regular tracks. A detailed on-top investigation was then performed on SSTs surfaces by using a Scanning Electron Microscope (SEM) PHENOM XL. To investigate the whole SST length, 5 micrographs were acquired for each SST. Furthermore, a comprehensive analysis of SSTs width ($w$) was conducted through ImageJ: for $i - th$ (with $i$ from 1 to 12) laser track the value $w_i$ was defined as the mean of 250 measurements.

**Table 2**
Laser power and scan speed values adopted for the SSTs analyzed to obtain the $P$-$v$ parameter combinations for AlSi10Mg + 4Cu alloy.

| Job | $P \times v$ matrix | $P$ [W] | $v$ [mm/s] |
|---|---|---|---|
| n°1 | 5 × 5 | 100, 130, 160, 180, 195 | 300, 600, 800, 1200, 1500 |
| n°2 | 3 × 4 | 160, 170, 180 | 700, 800, 900, 1000 |

### 2.3. Production and characterization of massive samples

Table 3 summarizes the range of the main process parameters adopted in the production of parallelepipeds with dimensions of 10 mm × 10 mm × 5 mm. Samples were produced by using a layer thickness of 30 μm. The building platform was preheated at 100 °C. As reported by Calignano et al. [16], with the LPBF system adopted in the present study, many scanning strategies could be adopted. For the first job, it was decided to employ the unidirectional scanning strategy, to clearly understand the effect of the variations of laser power, scanning speed and hatching distance on porosity content and on the overlapping of SSTs. Moreover, a full factorial DOE based on 2 factors ($P$ and $h_d$) with 3 levels and 1 factor ($v$) with 4 levels was chosen for a total of 36 combinations. $P$ and $v$ were adopted from the second job of SSTs, while to define the $h_d$ values it was decided to adopt Eq. (1), already used by Nie et al. [22]:

$$\varphi = \frac{w - h_d}{w} \cdot 100 \quad (1)$$

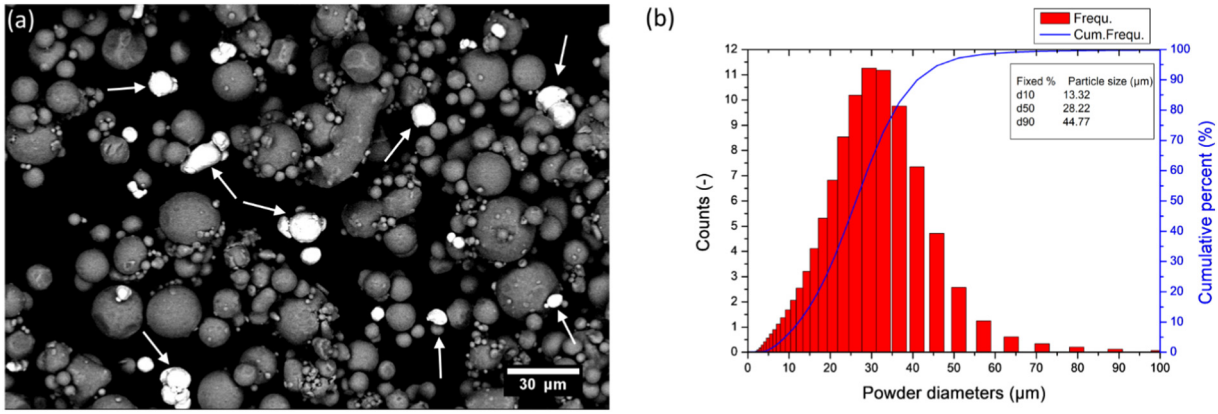


**Fig. 1.** (a) The AlSi10Mg + 4Cu mixed powder observed by FESEM in backscatter mode and (b) its particle size distribution with volumetric assumption.

**Table 3**
The range of factors and levels used for the DOE of the two jobs to manufacture parallelepiped samples.

| Job | Scanning strategy | $P \times v \times h_d$ matrix | $P$ [W] | $v$ [mm/s] | $h_d$ [mm] |
|---|---|---|---|---|---|
| n°1 | Unidirectional, 0° | $3 \times 4 \times 3$ | 160, 170, 180 | 700, 800, 900, 1000 | 0.08, 0.12, 0.14 |
| n°2 | Rotated, 67° | $2 \times 4 \times 2$ | 170, 180 | 700, 800, 900, 1000 | 0.12, 0.14 |

where $\varphi$ is the overlapping grade between nearby single tracks. In this way it was possible to fix three values of $h_d$ obtaining different overlapping conditions $\varphi$, namely completely overlapped ($\varphi > 20\%$), partially overlapped ($0\ \% \le \varphi \le 20\%$) and not-overlapped tracks ($\varphi < 0\%$), to check the quality of samples produced. In particular, considering the variability of $w_i$ of the SSTs produced in the second job, it was decided to use in Eq. (1) the width $\overline{w} = \sum w_i/12$.

To determine the density of the manufactured parallelepipeds, as-built samples were detached from the building platform using an electrical discharge machining (EDM) system. The samples outer surface was removed by grinding with SiC abrasive papers. Afterward, the density was evaluated in accordance with the Archimede's principle by using a Sartorius density measuring set YDK 01 [29], with 3 measurements for each sample. As theoretical density of the AlSi10Mg + 4Cu alloy, a value of 2.74 kg/dm$^3$ was estimated by using the volumetric rule of mixtures (ROM) [30]. All the data collected from the first job were analyzed using the statistical analysis software Minitab 17. Global analysis of variance (ANOVA) was applied to investigate parameters with significant effects on porosity. A significance level ($p$-$value$) < 0.005 was chosen. In addition, the cross-section along the building direction and perpendicular to the strategy direction for each specimen was polished down to 1 μm and investigated by OM to examine the presence of internal defects, e.g. pores, un-melted powder particles, and eventually cracks.

Then, a second job adopting a 67° rotated scanning strategy was planned. As reported in a previous study by Manfredi et al., this leads to isotropic properties in the plane parallel to the building platform [31]. In this case, a full factorial DOE with a restricted operating window, arising from the results of the first job, based on 2 factors ($P$ and $h_d$) with 2 levels and 1 factor ($v$) with 4 levels was designed. Again, all the samples were subjected to Archimede's density analysis in order to evaluate the porosity content. The microstructure was then investigated by means of SEM and a fully integrated Energy Dispersive X-ray Spectroscopy (EDS) detector of PHENOM XL. Hence, on the polished surface Brinell hardness (HB10) was evaluated applying a load of 62.5 kg using a hardness tester EMCO TEST M4U 025. On each sample, 5 measurements were performed according to ASTM E10-18 [32], in order to have a preliminary insight on the mechanical properties of the obtained AlSi10Mg + 4Cu parallelepipeds. Furthermore, also the productivity was considered and the build-up rates were estimated.

## 3. Results

### 3.1. Single scan tracks

Fig. 2a shows the top surfaces of SSTs produced in the first job (see Table 2). Over the entire range of parameters, two types of scan tracks can be recognized:

I) Unstable SSTs. At low laser powers, SSTs resulted to a large extent in irregular surfaces. Under the lowest scanning speed, the applied laser energy was sufficient to melt the powder to a significant extent, but top-surfaces exhibited spiked traces of partially melted material along the sides, as shown in Fig. A2a–b. As the scanning speed was increased, tracks showed a tendency to be more discontinuous and a preliminary balling phenomenon arise. Here, pronounced bulged balls followed by tight necking areas were clearly visible on SSTs surfaces (Fig. A2c). Finally, at 1500 mm/s and 100 W, the laser track splitted into separated drops, caused by the limited amount of liquid formed because the energy of laser input decreased (Fig. A2d).
II) Stable SSTs. At high laser powers, with the whole range of applied scanning speeds, a sufficient amount of liquid formed and yielded continuous and regular molten cylinders, free of pronounced balls.

Even though some tracks classified as stable show minor defects, e.g. a slightly marked hump effect at 180 W - 800 mm/s (Fig. A2e) and a wide heat affected zone at 195 W–300 mm/s (Fig. A2f), they could be considered acceptable at this stage since this on-top analysis aimed to verify the presence of macro-defects on SSTs surfaces. Then, a detailed investigation on melt pool cross-sections was carried out.

In Fig. 2b shape differences among the investigated melt pools are highlighted, while in Table A1 the dimensions of the geometrical features of melt pools are summarized. As can be observed in Fig. 2b, melt pools can be classified as irregular and regular:

I) Irregular melt pools. When the applied power was relatively low at scanning speeds up to 1200 mm/s, the laser energy was insufficient to fully melt the underlying substrate and, as a result, shallow melt pools with bumpy shape were generated. In these cases, melt pools were characterized by a $h/w$ ratio ≥ 0.63, which means that the shape is close to the spherical one. Furthermore, these melt pools had both significantly asymmetrical position on the substrate, with a $g/d$ ratio ≥ 1.47, together with a poor penetration. On the other hand, with the highest scanning speed, i.e. 1500 mm/s, and power values up to 160 W, the laser radiation interacted with the powder bed for a short time resulting in splashed melt pools with extremely low growth. In addition, using a laser power of 195 W with the lowest and highest speeds, irregular melt pools formed: in the first case, a deep and convex shaped melt pool with a markedly high $d$ value appeared, which means that a huge amount of energy density is applied; in the second case, the melt pool shape was more spherical with a reduced penetration, as a consequence of a shorter laser-material interaction.
II) Regular melt pools. By using power values ranging from 160 to 195 W, quite regular melt pools were formed. It is evident from the results that all such melt pools developed quasi-elliptical profiles, having a $h/w$ ratio between 0.39 and 0.62. Among these, two melt pools with the optimum shape were identified (see the green box in Fig. 2b). In fact, when the applied laser power is 160 or 180 W, at a scanning speed of 800 mm/s, symmetrical melt pools with $g/d$ ratio, respectively equal to 1.06 and 1.14, were produced.

As a result of the first SSTs job, the processing map of Fig. 3 was obtained, in which three different scenarios were identified. Firstly, the unstable SSTs - irregular melt pools scenario arise, where the laser energy was not efficiently absorbed by the powder, creating laser tracks with visible defects and melt pools with a pronounced asymmetry on the substrate. These building parameters were excluded for further trials. Secondly, stable SSTs with irregular melt pools were obtained at certain values of power and speed, corresponding to the yellow regions in Fig. 3. Here, the applied energy

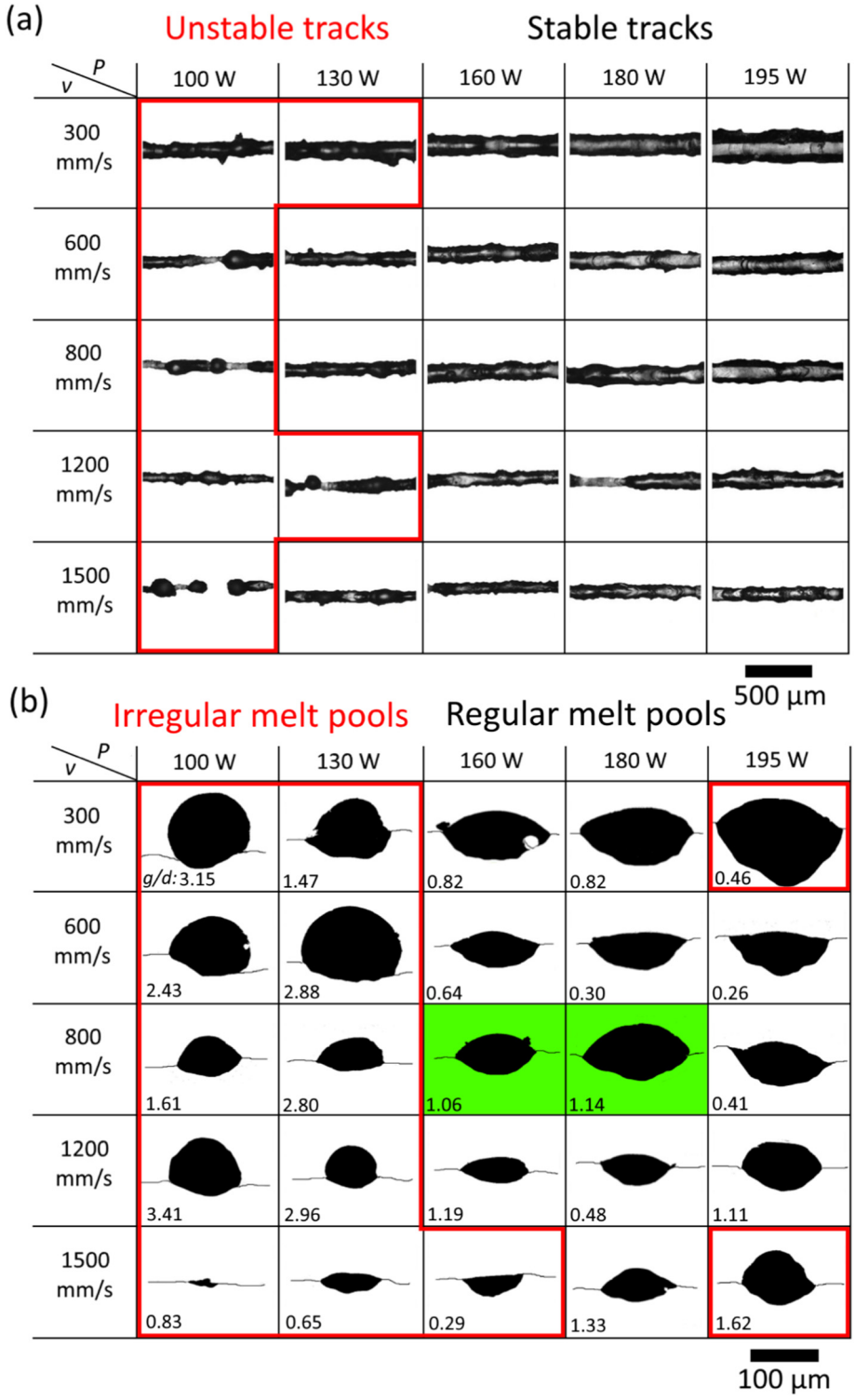


**Fig. 2.** (a) On-top surfaces and (b) melt pool cross-sections of single scan tracks produced in the first job.

was sufficient to preserve the scan track continuity, but shallow, splashed or convex melt pools were formed. Finally, the stable SSTs - regular melt pools scenario corresponds to the good *P*-*v* combinations for the investigated alloy. Within this scenario, *P*-*v* couples with values of 160 W–800 mm/s and 180 W–800 mm/s (see the dotted line in Fig. 3) were fixed as the starting point in designing the second SSTs job (see Table 2).

Fig. 4 illustrates SEM micrographs of the second job SSTs surfaces. As expected, macro-defects, such as ripples, distortions, and droplets, were not present. All the investigated SSTs showed an appreciable continuity, nevertheless, varied scan track morphologies can be observed. A few partially melted powder particles and laser-induced melt splashes were identified at 160 W–800 mm/s and 170 W–700 mm/s. Other laser tracks produced with 160 or 170 W

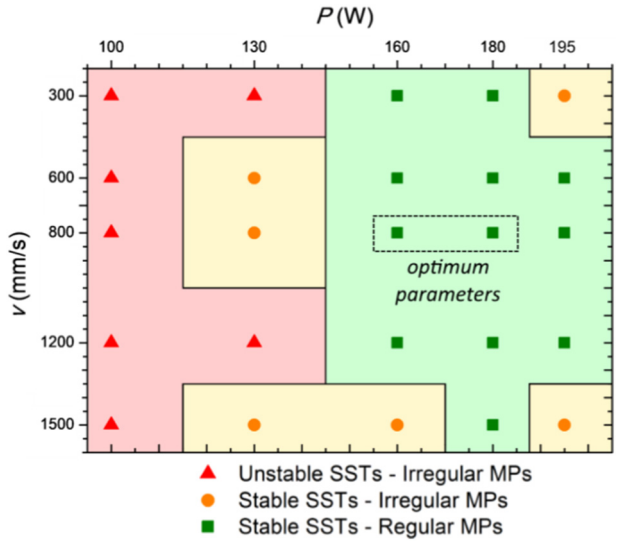


**Fig. 3.** Processing map of the AlSi10Mg + 4Cu alloy for the estimation of building process parameters effects.

were relatively smooth and linear. By increasing the laser power to 180 W, the SSTs continuity was well preserved, but they presented a bulging surface. In agreement with literature, this occurs especially when the LED increases and, therefore, the melt pool viscosity decreases [33]. Width values $w_i$ of all the SSTs were determined and reported as labels in Fig. 4, in correspondence to each SEM micrograph, with the related standard deviation.

### 3.2. Parallelepiped massive samples

Being all the SSTs produced in the second job regular and stable, by using the width value $\overline{w}$ equal to 131 μm in Eq. (1), $h_d$ values of 0.08, 0.12, 0.14 mm were adopted in the production of massive samples with unidirectional scanning strategy. The results of density analysis are summarized in Table A2. The values varied between 95.66 and 99.30%. In Table A3 the analysis of variance on porosity content is summarized. In this regard, ANOVA results revealed that the influence of power and hatching distance on the amount of porosity was highly significant, as they showed very low *p*-values. Both of these effects can be also appreciated by observing the main interaction plots reported in Fig. 5. In Fig. 5a, an increase in porosity by increasing *v* can be noticed. The porosity values of samples obtained at 160 W were always the highest and they decrease as the applied *P* increased, regardless of the applied scanning speed. In Fig. 5b, it could be observed that by using a $h_d$ of 0.08 mm, the highest porosity values were obtained in each *P* series. On the other hand, when $h_d$ increases, an appreciable reduction in porosity is achieved.

Fig. 6 shows the porosity values as a function of the SSTs $\varphi$ at different applied power levels. The three overlapping scenarios are superimposed on graphs of Fig. 6. Samples with higher density fall within the partially overlapped scenario, whereas specimens with lower density were produced with parameters belonging to not-overlapped and even completely-overlapped zones.

The polished cross-sections of samples built at 900 mm/s illustrated as an example in Fig. 7 suggested that in the not-overlapped scenario, aligned process porosities arise as a consequence of farther SSTs (see $a^i$). On the other hand in the completely overlapped scenario, an excessive laser re-melting generated unstable melt pool and the subsequent formation of irregular porosities.

On the basis of the previous results, *P* and $h_d$ values of 160 W and 0.08 mm, respectively, were excluded for the second job to manufacture parallelepiped samples with 67° rotated scanning strategy, as they implied porosity values higher than 1.50% (see Table A2). Table A4 summarizes density results, which varied from 98.62 to 99.16%, and the corresponding residual porosities, comprised in a narrow range, i.e. from 0.84 to 1.38%, are plotted as a function of the applied scanning speed in Fig. 8. This graph suggests that in this process window the effect of *P*, *v* and $h_d$ on porosity was negligible.

HB10 mean values together with standard deviation are listed in Table A4. Hardness varied from 137.0 ± 2.3 to 149.2 ± 2.0 HB, this variation cannot be attributed solely to a different porosity content. Considering for AlSi10Mg a reference hardness of 128.6 ± 1.9 HB [34], an increment between 6.5 and 16% was obtained, due to in-situ AlSi10Mg + 4Cu alloying and to the subsequent formation of Al(Cu) solid solution.

Fig. 9 shows the relationships among hardness, volumetric energy density (*VED*) and build-up rate ($\dot{V}$), determined according to Eqs. (2) and (3), respectively [35,36]:

$$VED = \frac{P}{v \cdot h_d \cdot t} \left[\frac{J}{mm^3}\right] \quad (2)$$

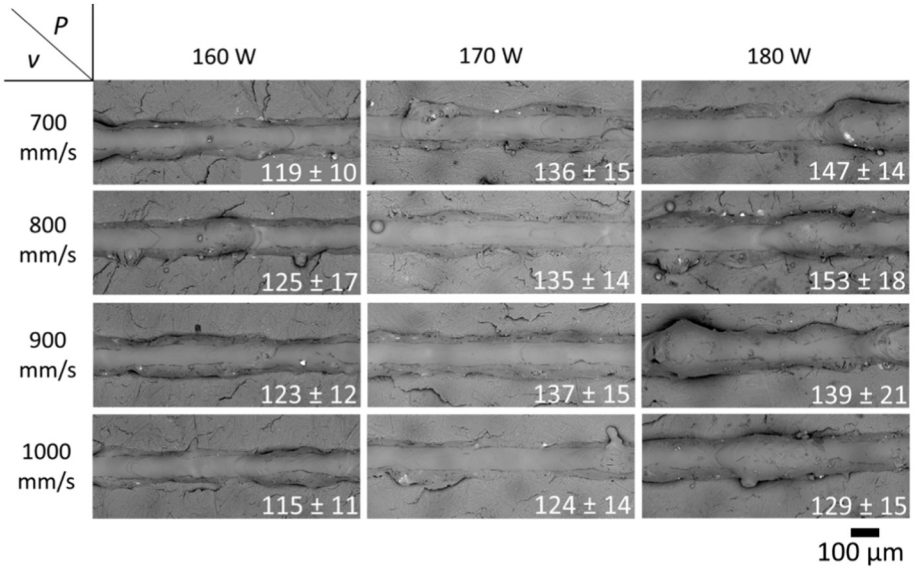


**Fig. 4.** SEM micrographs of SST surfaces in the second job. Width values $w_i$ of single tracks are labelled on the bottom-right side of each *P* - *v* box.

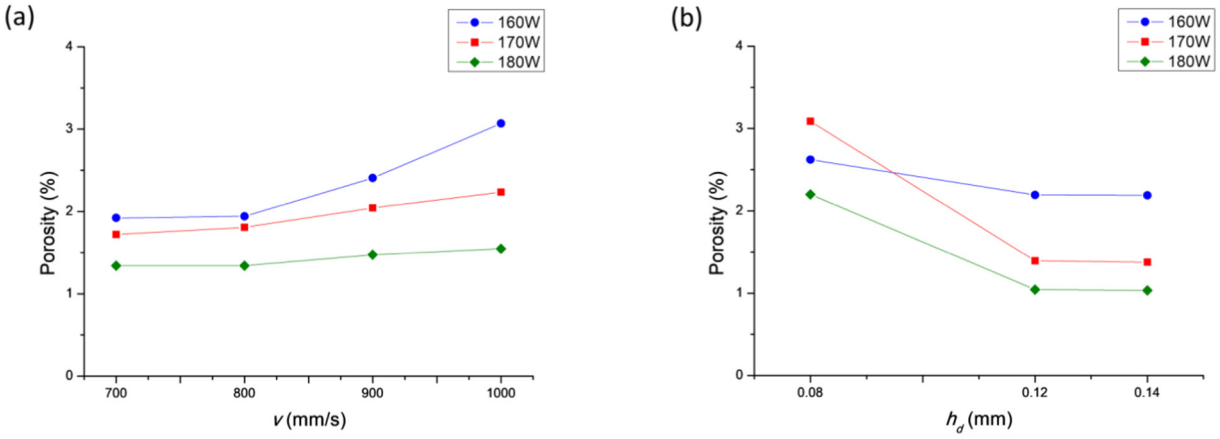


**Fig. 5.** Main interaction plots for porosity. (a) Relationship between porosity and scanning speed at varied power levels; (b) porosity values vs. hatching distance according to the used power.

$$\dot{V} = v \cdot h_d \cdot t \left[\frac{cm^3}{h}\right] \quad (3)$$

where $t$ is the layer thickness fixed at 0.03 mm in this study. The obtained data are reported in Table A4. In Fig. 9, a general reduction of hardness on growing *VED* is evident. On the other hand, the higher the *VED* the lower the build-up rate.

## 4. Discussion

### 4.1. LPBF of AlSi10Mg + 4Cu alloy

By using AlSi10Mg + 4Cu mixed powder, SSTs were at first produced in order to verify quickly the alloy processability and, on the basis of on-top and cross-section analyses, to define *P-v* combinations

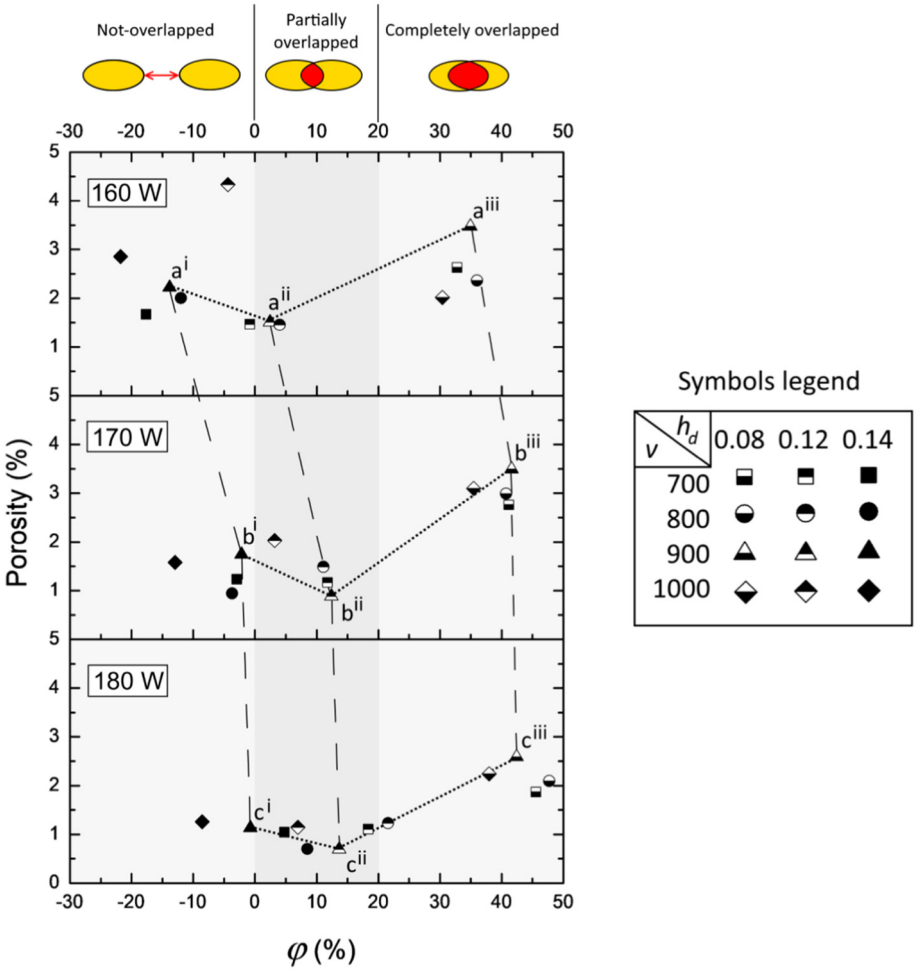


**Fig. 6.** Effect of $\varphi$ on porosity values of AlSiMg+4Cu unidirectional massive samples. Dotted and dashed lines refer respectively to the iso-power and iso-hatching behaviors at 900 mm/s.

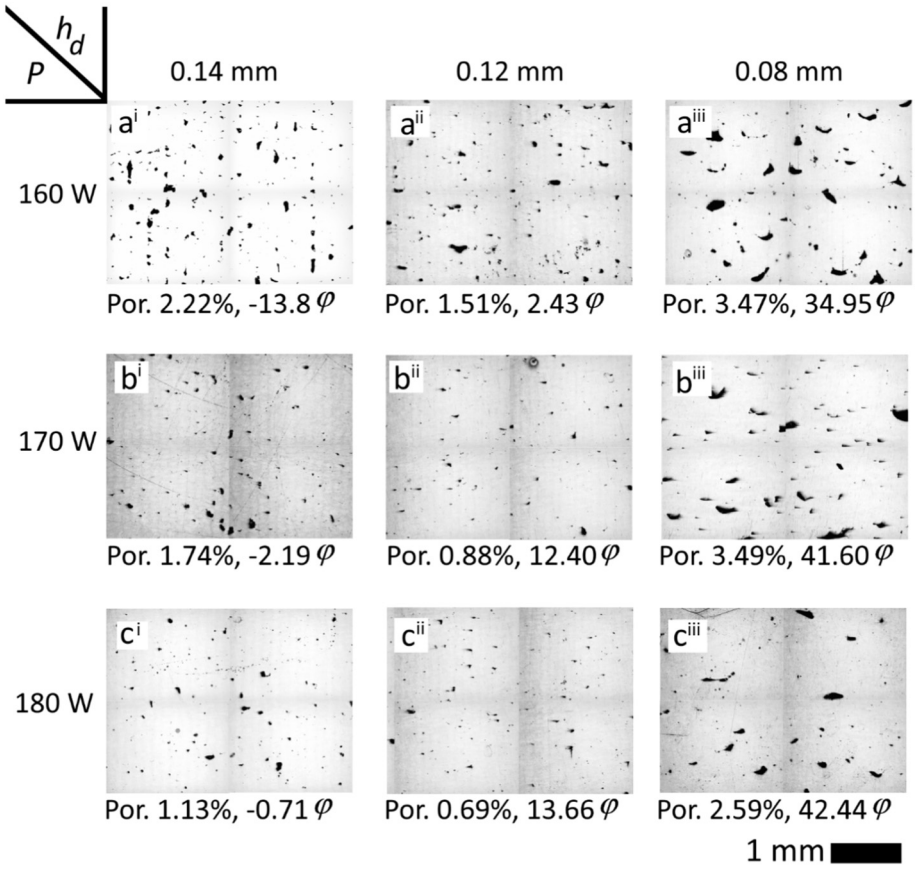


**Fig. 7.** Cross-sections of samples with unidirectional scanning strategy at 900 mm/s. The label on the top-left of each P - $h_d$ box refers to the labelled points showed in Fig. 6.

for stable and regular SSTs (Fig. 3). Then, an additional job was performed to finely tune the process parameters. SSTs widths were evaluated: notwithstanding a certain variability in $w_i$ values labelled for each specific *P-v* combinations in Fig. 4, for a given scanning speed, $w_i$ values increase as the power increases, following a similar trend as reported in Fig. 10. For this reason Authors decided to adopt $\overline{w}$ in order to determine three $h_d$ values for the production of parallelepiped massive samples.

The porosity data related to specimens with unidirectional scanning strategy, plotted in Fig. 6, can be analyzed focusing the attention on iso-power (dotted lines) and iso-hatching (dashed lines) behaviors. In the first case, porosity reaches the minimum in the partially overlapped scenario for all *P* series (see $a^{ii}$, $b^{ii}$ and $c^{ii}$). On the other hand, considering the iso-hatching behaviors, it can be pointed out that φ increases as the applied *P* increases. Interestingly, this correlation is in agreement with the linear relationship between $w_i$ and *P* provided in Fig. 10. Increasing *P* and, consequently, increasing φ was found beneficial in term of density: following the iso-hatching behaviour at 0.14 mm porosity values are reduced from 2.22% of $a^i$ to 1.13% of $c^i$. Considering the iso-hatching behaviour at 0.12 mm, a porosity below 1.50% is always obtained. Finally, in the case of iso-hatching at 0.08 mm, a higher amount of large porosities appears. The process window selected for the production of massive samples with 67° rotated scanning strategy revealed to be suitable for the main goal of developing a new alloy for LPBF: high density values near the theoretical one are obtained in all cases. In addition, the EDS analysis map of Fig. 11 revealed a quite uniform distribution of Cu within the Al matrix, confirming the effectiveness of processing mixed powders by LPBF.

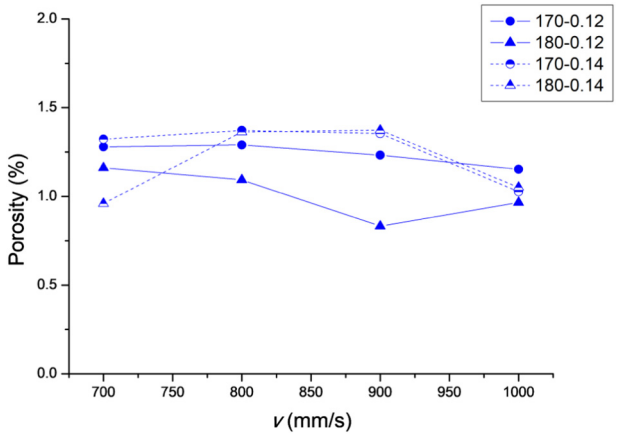


**Fig. 8.** Variation of porosity with the applied scanning speeds for the second job of parallelepiped AlSi10Mg + 4Cu samples.

Therefore the choice of the proper main process parameters relies on the final aim: hardness or productivity? When high build-up rate is needed, a $h_d$ of 0.14 mm and a *v* of 1000 mm/s must be used, while if the highest hardness is wanted, a *P* of 180 W, a $h_d$ of 0.12 mm and a *v* of 1000 mm/s must be used.

### 4.2. New method for the definition of LPBF parameters

*At posteriori* analysis of the above experimental results supports the definition of a method for a time and cost-effective identification of the main process parameters to manufacture new alloys for LPBF. According to the particle size distribution of the powder, the layer thickness is fixed. After that, as already demonstrated in literature [9,17–22], the proper *P-v* combinations are identified through SSTs approach. In particular, in the work of Nie et al. [22], the process window is then completed by producing and characterizing multi tracks for the definition

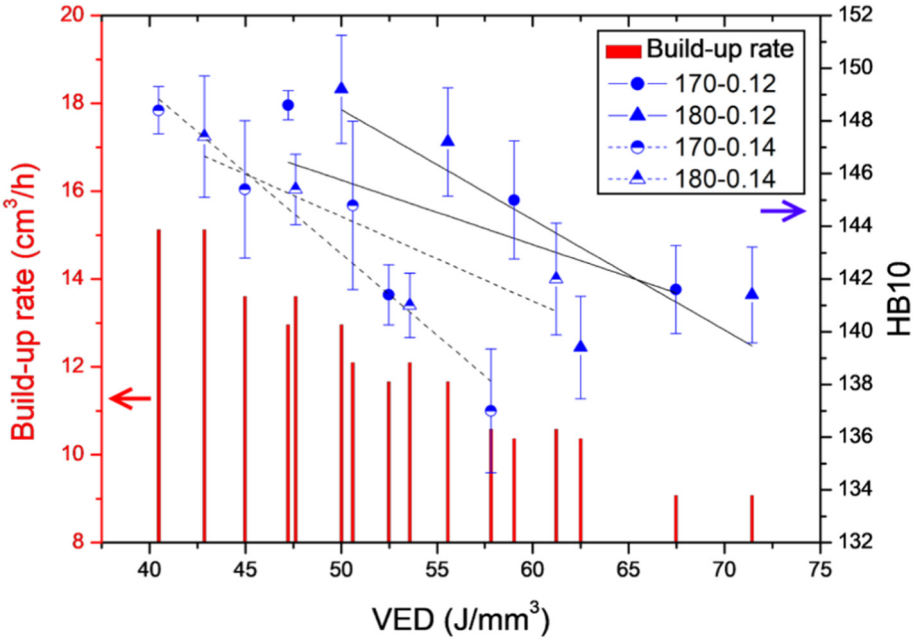


**Fig. 9.** Significant relationships between hardness, build-up rate and *VED* for the AlSi10Mg + 4Cu massive samples with 67° rotated scanning strategy.

of hatching distance. On the other hand, according to the innovative methodology proposed in this study, through SST jobs also the $h_d$ value is defined.

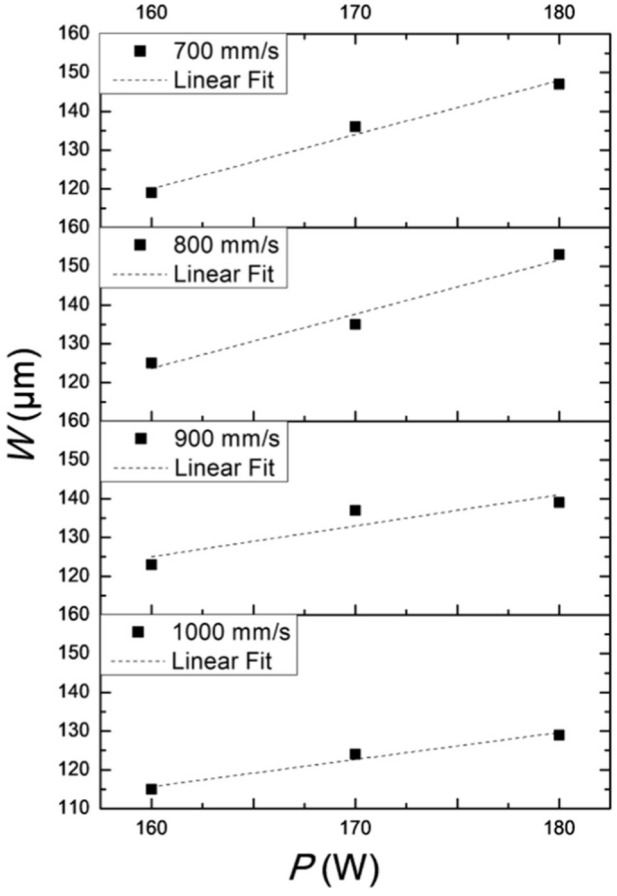


**Fig. 10.** Significant relationships between SSTs width and laser power at different scanning speeds.

As previously demonstrated, $h_d$ can be calculated by using the reverse function of Eq. (1), i.e. the following Eq. (4):

$$h_d = w \cdot \left(1 - \frac{\varphi}{100}\right) \tag{4}$$

To minimize residual porosity it is necessary to stay in the partially overlapped scenario (see Fig. 6). For this reason, by using in Eq. (4) $\varphi$ values ranged between 0 and 20% and the specific SST width $w_i$, taking into account the correlation between scan width and *P-v* combinations, $h_d$ values can be identified. In this way, just through the SSTs characterization a narrow process window for the production of massive samples with 67° rotated scanning strategy can be selected. *P*, *v* and also $h_d$ to be used in DOE are then defined without producing samples with unidirectional scanning strategy, minimizing the number of the samples produced and accelerating times. To validate this novel methodology, the main process parameters adopted in previous studies for the AlSi10Mg powder with the same LPBF system were considered [31]. Hence, a single scan track of AlSi10Mg was produced at 195 W and 800 mm/s with the procedure explained in Section 2.2. Then, SST width was determined and its value was found to be 170 ± 14 µm. Interestingly, by using in Eq. (1) the determined SST width and a $h_d$ of 0.17 mm [31], a $\varphi$ value of 0% was obtained, confirming the role of overlapping here suggested.

## 5. Conclusions

The present work aimed to pursue two main goals: on one side, a mixed AlSi10Mg + 4Cu powder was processed through LBPF to produce SSTs and then massive parallelepiped samples; on the other side, on the basis of the experimental analysis, a method for processing new alloys was defined and proposed. Specifically, the experimentally findings of this study can be summarized as follows:

1) a reliable *P-v* window, characterized by stable SSTs and regular melt pools, is determined for the AlSi10Mg + 4Cu alloy by quickly analysing SSTs on-top and cross-section surfaces;
2) fixed the layer thickness, in relations to the powder size and distribution, and defined $h_d$ on the basis of overlapping, parallelepiped

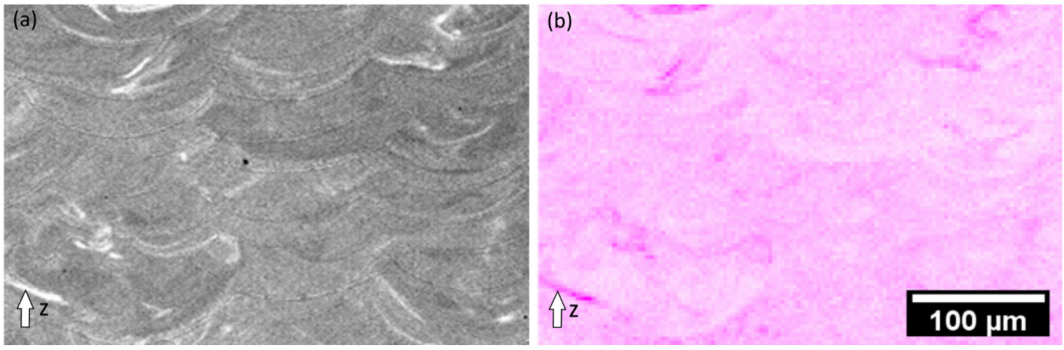


**Fig. 11.** EDS analysis performed on massive sample with 67° rotated scanning strategy: (a) SEM micrograph of a polished cross-section along the building direction, as indicated by the white arrow; (b) elemental map of the Cu distribution.

massive samples with unidirectional scanning strategy were produced and characterized in terms of density;

3) AlSi10Mg + 4Cu samples produced using 67° rotated scanning strategy and $\varphi$ in the range of 0–20% showed density level up to 99.16%;
4) in terms of mechanical properties, Cu addition to AlSi10Mg alloy provided an increment of hardness between 6.5 and 16%, depending on the applied VED;
5) when high build-up rate is needed, a $h_d$ of 0.14 mm and a $v$ of 1000 mm/s must be used, while if the highest hardness is wanted, a $P$ of 180 W, a $h_d$ of 0.12 mm and a $v$ of 1000 mm/s must be used.

Therefore it was demonstrated how near fully dense samples made of a new alloy can be obtained through an accelerated definition of the main LPBF process parameters, which involves few steps, saving time and powders. In fact, imposing $\varphi$ values ranged between 0 and 20% and measuring the specific SST width $w_i$, $h_d$ values are easily defined. In this way producing and characterizing SSTs the main process parameters for the production of samples with 67° rotated scanning strategy are directly established.

## Data availability

The authors declare that the main data supporting the findings of this work are available within the article and in Appendix A.

## CRediT authorship contribution statement

**Federico Bosio:** Conceptualization, Methodology, Validation, Investigation, Data curation, Writing - original draft, Writing - review & editing, Visualization. **Alberta Aversa:** Methodology, Validation, Investigation, Data curation. **Massimo Lorusso:** Investigation, Data curation. **Silvia Marola:** Investigation. **Dario Gianoglio:** Investigation. **Livio Battezzati:** Supervision, Writing - review & editing. **Paolo Fino:** Supervision, Project administration, Funding acquisition. **Diego Manfredi:** Conceptualization, Writing - review & editing, Supervision. **Mariangela Lombardi:** Conceptualization, Writing - review & editing, Supervision, Project administration, Funding acquisition.

## Acknowledgments

The authors would like to acknowledge the regional project STAMP (Sviluppo Tecnologico dell'Additive Manufacturing in Piemonte).

## Appendix A

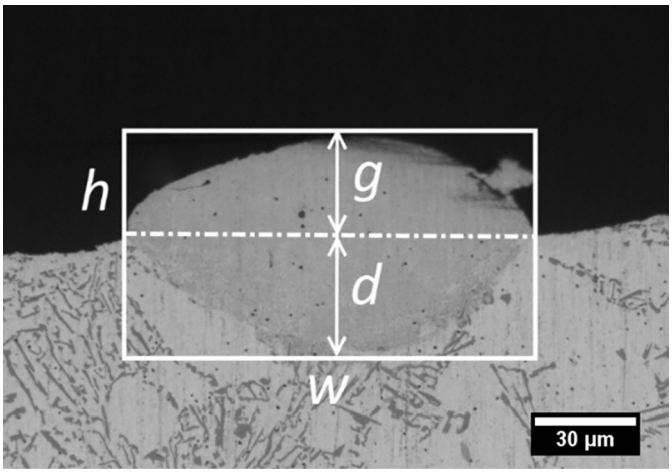


**Fig. A1.** Scheme of the melt pool cross-section with the dimensions used to determine the melt pool geometrical features. The investigated melt pool geometrical features are width ($w$), total height ($h$), growth ($g$) and penetration in the substrate ($d$). The obtained aspect-ratio indicators are the height to width ratio ($h/w$) and the growth to depth ratio ($g/w$).

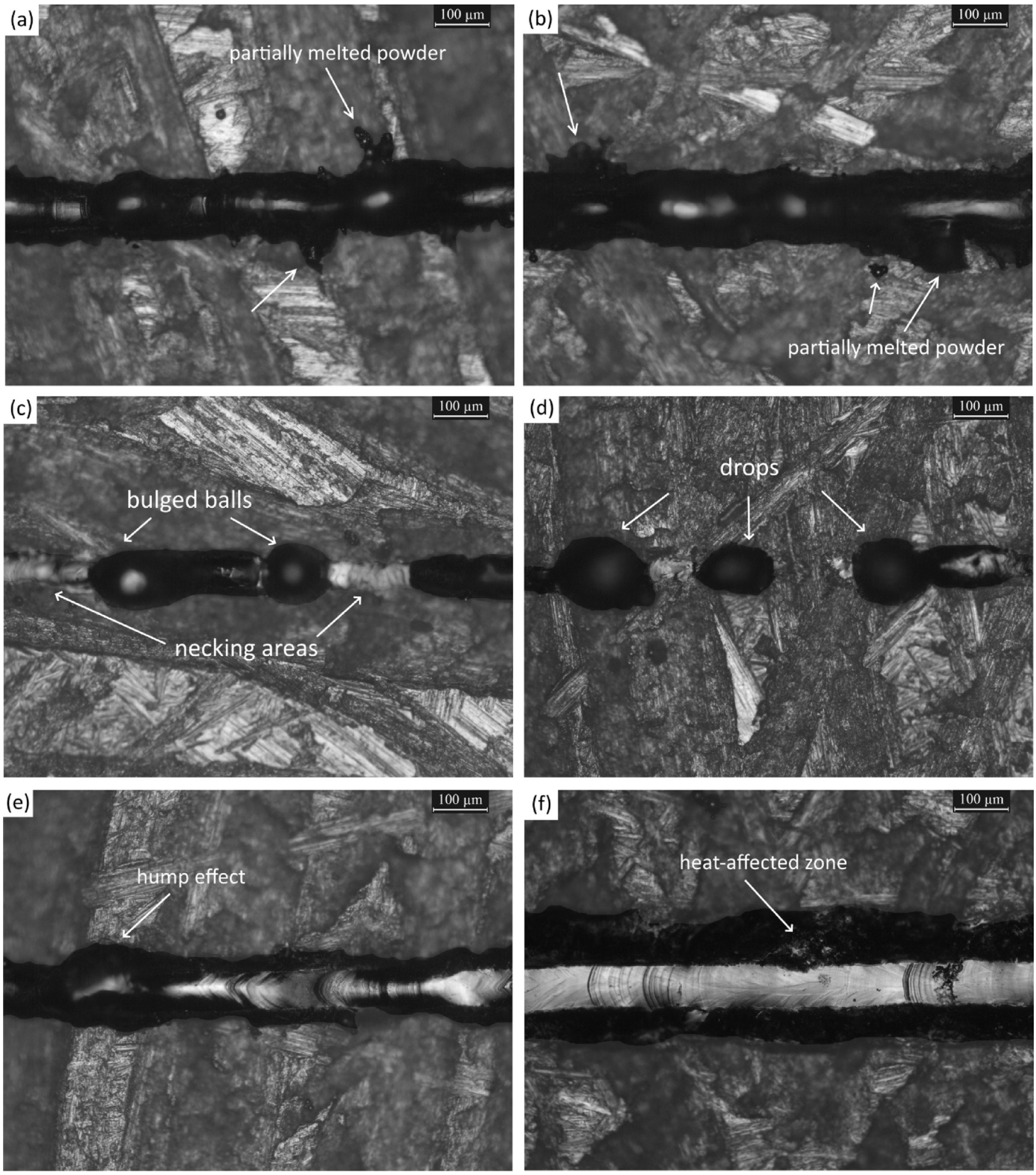


**Fig. A2.** Irregularities observed on AlSi10Mg + 4Cu on-top surfaces built with (a) 100 W and (b) 130 W at a constant scanning speed of 300 mm/s; (b) 800 mm/s and (d) 1500 mm/s at a constant laser power of 100 W; (e) 180 W–800 mm/s; (f) 195 W-300 mm/s.

**Table A1**
Results of the quantitative analysis on melt pool cross-sections. Geometrical characteristics are determined according to Fig. A1.

| *P* [W] | *v* [mm/s] | *LED* [J/mm] | *w* [μm] | *h* [μm] | *h*/*w* [-] | *g* [μm] | *d* [μm] | *g*/*d* [-] |
|---|---|---|---|---|---|---|---|---|
| 100 | 300 | 0.33 | 134 | 92.56 | 0.68 | 70.26 | 22.30 | 3.15 |
| | 600 | 0.16 | 120 | 90.96 | 0.74 | 64.45 | 26.51 | 2.43 |
| | 800 | 0.12 | 96 | 61.45 | 0.63 | 37.94 | 23.51 | 1.61 |
| | 1200 | 0.08 | 107 | 87.35 | 0.81 | 67.55 | 19.80 | 3.41 |
| | 1500 | 0.06 | 45 | 13.43 | 0.30 | 6.10 | 7.33 | 0.83 |
| 130 | 300 | 0.43 | 128 | 91.93 | 0.70 | 54.65 | 37.28 | 1.47 |
| | 600 | 0.21 | 148 | 113.44 | 0.76 | 84.23 | 29.21 | 2.88 |
| | 800 | 0.16 | 101 | 50.33 | 0.49 | 37.09 | 13.24 | 2.80 |
| | 1200 | 0.10 | 78 | 63.29 | 0.82 | 47.29 | 16 | 2.96 |
| | 1500 | 0.08 | 91 | 31.12 | 0.34 | 12.21 | 18.91 | 0.65 |
| 160 | 300 | 0.53 | 169 | 74.28 | 0.44 | 33.52 | 40.76 | 0.82 |
| | 600 | 0.26 | 132 | 55.02 | 0.41 | 21.50 | 33.52 | 0.64 |
| | 800 | 0.2 | 120 | 62.36 | 0.51 | 32.12 | 30.24 | 1.06 |
| | 1200 | 0.13 | 95 | 54.75 | 0.57 | 29.77 | 24.98 | 1.19 |
| | 1500 | 0.10 | 91 | 36.02 | 0.39 | 8.18 | 27.84 | 0.29 |
| 180 | 300 | 0.6 | 168 | 88.1 | 0.52 | 39.72 | 48.38 | 0.82 |
| | 600 | 0.3 | 145 | 57.08 | 0.39 | 13.05 | 44.03 | 0.30 |
| | 800 | 0.22 | 155 | 83.92 | 0.54 | 44.77 | 39.15 | 1.14 |
| | 1200 | 0.15 | 111 | 46.81 | 0.42 | 15.23 | 31.58 | 0.48 |
| | 1500 | 0.12 | 108 | 50.25 | 0.46 | 28.70 | 21.55 | 1.33 |
| 195 | 300 | 0.65 | 187 | 131.44 | 0.70 | 41.15 | 90.29 | 0.46 |
| | 600 | 0.32 | 148 | 67.14 | 0.45 | 13.90 | 53.24 | 0.26 |
| | 800 | 0.24 | 156 | 66.59 | 0.43 | 19.39 | 47.20 | 0.41 |
| | 1200 | 0.16 | 117 | 73.36 | 0.62 | 38.55 | 34.81 | 1.11 |
| | 1500 | 0.13 | 109 | 82.15 | 0.75 | 50.77 | 31.38 | 1.62 |

**Table A2**
Results of density analysis for all the parameters considered in the DoE of AlSi10Mg + 4Cu parallelepiped samples by LPBF with unidirectional scanning strategy.

| *P* [W] | *v* [mm/s] | $h_d$ [mm] | $\rho_{Arch.}$ [Kg/dm$^3$] | $\rho_{Rel.}$ [%] | Porosity [%] | $\varphi$ [%] |
|---|---|---|---|---|---|---|
| 160 | 700 | 0.08 | 2.67 | 97.38 | 2.62 | 32.77 |
| | | 0.12 | 2.70 | 98.54 | 1.46 | −0.84 |
| | | 0.14 | 2.69 | 98.33 | 1.67 | −17.65 |
| | 800 | 0.08 | 2.67 | 97.64 | 2.36 | 36.00 |
| | | 0.12 | 2.70 | 98.55 | 1.45 | 4.00 |
| | | 0.14 | 2.68 | 98.00 | 2.00 | −12.00 |
| | 900 | 0.08 | 2.64 | 96.53 | 3.47 | 34.95 |
| | | 0.12 | 2.70 | 98.49 | 1.51 | 2.43 |
| | | 0.14 | 2.68 | 97.78 | 2.22 | −13.82 |
| | 1000 | 0.08 | 2.68 | 97.99 | 2.01 | 30.44 |
| | | 0.12 | 2.62 | 95.67 | 4.33 | −4.35 |
| | | 0.14 | 2.66 | 97.15 | 2.85 | −21.74 |
| 170 | 700 | 0.08 | 2.66 | 97.25 | 2.75 | 41.18 |
| | | 0.12 | 2.71 | 98.84 | 1.16 | 11.77 |
| | | 0.14 | 2.71 | 98.77 | 1.23 | −2.94 |
| | 800 | 0.08 | 2.66 | 97.01 | 2.99 | 40.74 |
| | | 0.12 | 2.70 | 98.52 | 1.48 | 11.11 |
| | | 0.14 | 2.71 | 99.06 | 0.94 | −3.70 |
| | 900 | 0.08 | 2.64 | 96.51 | 3.49 | 41.60 |
| | | 0.12 | 2.71 | 99.12 | 0.88 | 12.40 |
| | | 0.14 | 2.69 | 98.26 | 1.74 | −2.19 |
| | 1000 | 0.08 | 2.65 | 96.91 | 3.09 | 35.48 |
| | | 0.12 | 2.68 | 97.98 | 2.02 | 3.23 |
| | | 0.14 | 2.70 | 98.42 | 1.58 | −12.90 |
| 180 | 700 | 0.08 | 2.69 | 98.13 | 1.87 | 45.58 |
| | | 0.12 | 2.71 | 98.90 | 1.10 | 18.37 |
| | | 0.14 | 2.71 | 98.96 | 1.04 | 4.76 |
| | 800 | 0.08 | 2.68 | 97.91 | 2.09 | 47.71 |
| | | 0.12 | 2.71 | 98.78 | 1.22 | 21.57 |
| | | 0.14 | 2.72 | 99.31 | 0.69 | 8.50 |
| | 900 | 0.08 | 2.67 | 97.41 | 2.59 | 42.44 |
| | | 0.12 | 2.72 | 99.31 | 0.69 | 13.67 |
| | | 0.14 | 2.71 | 98.87 | 1.13 | −0.71 |
| | 1000 | 0.08 | 2.68 | 97.76 | 2.24 | 37.98 |
| | | 0.12 | 2.71 | 98.86 | 1.14 | 6.98 |
| | | 0.14 | 2.70 | 98.75 | 1.25 | −8.53 |

**Table A3**
Analysis of Variance (ANOVA) of the porosity content of AlSi10Mg + 4Cu samples produced by LPBF using unidirectional scanning strategy.

| Source | DF | Sum of squares | F-value | p-value | Statistical significance ($p < 0.005$) |
|---|---|---|---|---|---|
| $P$ | 2 | 4.990 | 9.73 | 0.003 | Significant |
| $v$ | 3 | 2.267 | 2.95 | 0.076 | Not significant |
| $h_d$ | 2 | 9.647 | 18.82 | 0.000 | Significant |
| $P \cdot v$ | 6 | 0.929 | 0.60 | 0.723 | Not significant |
| $P \cdot h_d$ | 4 | 2.172 | 2.12 | 0.141 | Not significant |
| $v \cdot h_d$ | 6 | 3.781 | 2.46 | 0.087 | Not significant |
| Error | 12 | 3.075 | | | |
| Total | 35 | 26.863 | | | |

**Table A4**
Porosity, Brinell hardness and Build up rate values of AlSi10Mg + 4Cu parallelepiped samples produced by LPBF with 67° rotated scanning strategy.

| $P$ [W] | $v$ [mm/s] | $h_d$ [mm] | $VED$ [J/mm$^3$] | Build-up rate [cm$^3$/h] | $\rho_{Arch.}$ [Kg/dm$^3$] | $\rho_{Rel.}$ [%] | Porosity [%] | HB10 |
|---|---|---|---|---|---|---|---|---|
| 170 | 700 | 0.12 | 67.46 | 9.07 | 2.70 | 98.72 | 1.27 | 141.6 ± 1.6 |
| | 800 | | 59.03 | 10.37 | 2.70 | 98.71 | 1.29 | 145.0 ± 2.2 |
| | 900 | | 52.47 | 11.66 | 2.71 | 98.76 | 1.23 | 141.4 ± 1.1 |
| | 1000 | | 47.22 | 12.96 | 2.71 | 98.84 | 1.15 | 148.6 ± 0.5 |
| 180 | 700 | | 71.43 | 9.07 | 2.71 | 98.83 | 1.16 | 141.4 ± 1.8 |
| | 800 | | 62.50 | 10.37 | 2.71 | 98.90 | 1.09 | 139.4 ± 1.9 |
| | 900 | | 55.56 | 11.66 | 2.72 | 99.16 | 0.83 | 147.2 ± 2.0 |
| | 1000 | | 50.00 | 12.96 | 2.71 | 99.03 | 0.96 | 149.2 ± 2.0 |
| 170 | 700 | 0.14 | 57.82 | 10.58 | 2.70 | 98.67 | 1.32 | 137.0 ± 2.3 |
| | 800 | | 50.60 | 12.10 | 2.70 | 98.62 | 1.37 | 144.8 ± 3.1 |
| | 900 | | 44.97 | 13.61 | 2.70 | 98.64 | 1.35 | 145.4 ± 2.6 |
| | 1000 | | 40.48 | 15.12 | 2.71 | 98.97 | 1.02 | 148.4 ± 0.8 |
| 180 | 700 | | 61.22 | 10.58 | 2.71 | 99.04 | 0.96 | 142.0 ± 2.1 |
| | 800 | | 53.57 | 12.10 | 2.70 | 98.63 | 1.36 | 141.0 ± 1.2 |
| | 900 | | 47.62 | 13.61 | 2.70 | 98.62 | 1.37 | 145.4 ± 1.3 |
| | 1000 | | 42.86 | 15.12 | 2.71 | 98.95 | 1.05 | 147.4 ± 2.3 |

## References


[1] D. Herzog, V. Seyda, E. Wycisk, C. Emmelmann, Additive manufacturing of metals, Acta Mater. 117 (2016) 371–392, https://doi.org/10.1016/j.actamat.2016.07.019.

[2] N. Li, S. Huang, G. Zhang, R. Qin, W. Liu, H. Xiong, G. Shi, J. Blackburn, Progress in additive manufacturing on new materials: a review, J. Mater. Sci. Technol. 35 (2018) 242–269, https://doi.org/10.1016/j.jmst.2018.09.002.

[3] T. DebRoy, H.L. Wei, J.S. Zuback, T. Mukherjee, J.W. Elmer, J.O. Milewski, A.M. Beese, A. Wilson-Heid, A. De, W. Zhang, Additive manufacturing of metallic components – process, structure and properties, Prog. Mater. Sci. 92 (2018) 112–224, https://doi.org/10.1016/j.pmatsci.2017.10.001.

[4] G. Kasperovich, J. Haubrich, J. Gussone, G. Requena, Correlation between porosity and processing parameters in TiAl6V4 produced by selective laser melting, Mater. Des. 105 (2016) 160–170, https://doi.org/10.1016/j.matdes.2016.05.070.

[5] S. Liu, Y.C. Shin, Additive manufacturing of Ti6Al4V alloy: a review, Mater. Des. 164 (2018) 107552, https://doi.org/10.1016/j.matdes.2018.107552.

[6] D. Wang, C. Song, Y. Yang, Y. Bai, Investigation of crystal growth mechanism during selective laser melting and mechanical property characterization of 316L stainless steel parts, Mater. Des. 100 (2016) 291–299, https://doi.org/10.1016/j.matdes.2016.03.111.

[7] H. Choo, K.-L. Sham, J. Bohling, A. Ngo, X. Xiao, Y. Ren, P.J. Depond, M.J. Matthews, E. Garlea, Effect of laser power on defect, texture, and microstructure of a laser powder bed fusion processed 316L stainless steel, Mater. Des. 164 (2018) 107534, https://doi.org/10.1016/j.matdes.2018.12.006.

[8] V.A. Popovich, E.V. Borisov, A.A. Popovich, V.S. Sufiiarov, D.V. Masaylo, L. Alzina, Functionally graded Inconel 718 processed by additive manufacturing: crystallographic texture, anisotropy of microstructure and mechanical properties, Mater. Des. 114 (2017) 441–449, https://doi.org/10.1016/j.matdes.2016.10.075.

[9] K. Kempen, L. Thijs, J. Van Humbeeck, J.-P. Kruth, Processing AlSi10Mg by selective laser melting: parameter optimisation and material characterisation, Mater. Sci. Technol. 31 (2015) 917–923, https://doi.org/10.1179/1743284714Y.0000000702.

[10] H. Rao, S. Giet, K. Yang, X. Wu, C.H.J. Davies, The influence of processing parameters on aluminium alloy A357 manufactured by Selective Laser Melting, Mater. Des. 109 (2016) 334–346, https://doi.org/10.1016/j.matdes.2016.07.009.

[11] Y. Brif, M. Thomas, I. Todd, The use of high-entropy alloys in additive manufacturing, Scr. Mater. 99 (2015) 93–96, https://doi.org/10.1016/j.scriptamat.2014.11.037.

[12] J.H. Martin, B.D. Yahata, J.M. Hundley, J.A. Mayer, T.A. Schaedler, T.M. Pollock, 3D printing of high-strength aluminium alloys, Nature 549 (2017) 365–369, https://doi.org/10.1038/nature23894.

[13] S.A.M. Tofail, E.P. Koumoulos, A. Bandyopadhyay, S. Bose, L. O'Donoghue, C. Charitidis, Additive manufacturing: scientific and technological challenges, market uptake and opportunities, Mater. Today 21 (2018) 22–37, https://doi.org/10.1016/j.mattod.2017.07.001.

[14] J.H. Tan, W.L.E. Wong, K.W. Dalgarno, An overview of powder granulometry on feedstock and part performance in the selective laser melting process, Addit. Manuf. 18 (2017) 228–255, https://doi.org/10.1016/j.addma.2017.10.011.

[15] A.T. Sutton, C.S. Kriewall, M.C. Leu, J.W. Newkirk, Powder characterisation techniques and effects of powder characteristics on part properties in powder-bed fusion processes, Virtual Phys. Prototyp. 12 (2017) 3–29, https://doi.org/10.1080/17452759.2016.1250605.

[16] F. Calignano, G. Cattano, D. Manfredi, Manufacturing of thin wall structures in AlSi10Mg alloy by laser powder bed fusion through process parameters, J. Mater. Process. Technol. 255 (2018) 773–783, https://doi.org/10.1016/j.jmatprotec.2018.01.029.

[17] D. Gu, Y. Shen, Balling phenomena during direct laser sintering of multi-component Cu-based metal powder, J. Alloys Compd. 432 (2007) 163–166, https://doi.org/10.1016/j.jallcom.2006.06.011.

[18] I. Yadroitsev, I. Smurov, Selective laser melting technology: from the single laser melted track stability to 3D parts of complex shape, Phys. Procedia 5 (2010) 551–560, https://doi.org/10.1016/j.phpro.2010.08.083.

[19] C. Li, Y.B. Guo, J.B. Zhao, Interfacial phenomena and characteristics between the deposited material and substrate in selective laser melting Inconel 625, J. Mater. Process. Technol. 243 (2017) 269–281, https://doi.org/10.1016/j.jmatprotec.2016.12.033.

[20] P. Wei, Z. Wei, Z. Chen, J. Du, Y. He, J. Li, Y. Zhou, The AlSi10Mg samples produced by selective laser melting: single track, densification, microstructure and mechanical behavior, Appl. Surf. Sci. 408 (2017) 38–50, https://doi.org/10.1016/j.apsusc.2017.02.215.

[21] A. Aversa, M. Moshiri, E. Librera, M. Hadi, G. Marchese, D. Manfredi, M. Lorusso, F. Calignano, S. Biamino, M. Lombardi, M. Pavese, Single scan track analyses on aluminium based powders, J. Mater. Process. Technol. 255 (2018) 17–25, https://doi.org/10.1016/j.jmatprotec.2017.11.055.

[22] X. Nie, H. Zhang, H. Zhu, Z. Hu, L. Ke, X. Zeng, Analysis of processing parameters and characteristics of selective laser melted high strength Al-Cu-Mg alloys: from single tracks to cubic samples, J. Mater. Process. Technol. 256 (2018) 69–77, https://doi.org/10.1016/j.jmatprotec.2018.01.030.

[23] B. Cheng, S. Shrestha, K. Chou, Stress and deformation evaluations of scanning strategy effect in selective laser melting, Addit. Manuf. 12 (2016) 240–251, https://doi.org/10.1016/j.addma.2016.05.007.

[24] M. Krishnan, E. Atzeni, R. Canali, F. Calignano, D. Manfredi, E.P. Ambrosio, L. Iuliano, On the effect of process parameters on properties of AlSi10Mg parts produced by DMLS, Rapid Prototyp. J. 20 (2014) 449–458, https://doi.org/10.1108/RPJ-03-2013-0028.

[25] J. Sun, Y. Yang, D. Wang, Parametric optimization of selective laser melting for forming Ti6Al4V samples by Taguchi method, Opt. Laser Technol. 49 (2013) 118–124, https://doi.org/10.1016/j.optlastec.2012.12.002.

[26] N. Read, W. Wang, K. Essa, M.M. Attallah, Selective laser melting of AlSi10Mg alloy: process optimisation and mechanical properties development, Mater. Des. 65 (2015) 417–424, https://doi.org/10.1016/j.matdes.2014.09.044.
[27] Z. Li, I. Kucukkoc, D.Z. Zhang, F. Liu, Optimising the process parameters of selective laser melting for the fabrication of Ti6Al4V alloy, Rapid Prototyp. J. 24 (2018) 150–159, https://doi.org/10.1108/RPJ-03-2016-0045.
[28] H. Yeung, B.M. Lane, M.A. Donmez, J.C. Fox, J. Neira, Implementation of advanced laser control strategies for powder bed fusion systems, Procedia Manuf 26 (2018) 871–879, https://doi.org/10.1016/j.promfg.2018.07.112.
[29] ASTM B962, Standard Test Methods for Density of Compacted or Sintered Powder Metallurgy (PM) Products Using Archimedes Principle, ASTM Int., 2013 1–7, https://doi.org/10.1520/B0962-13.2.
[30] D.R. Askeland, P.P. Fulay, W.J. Wright, The Science and Engineering of Materials, Third S.I. 1998.
[31] D. Manfredi, F. Calignano, M. Krishnan, R. Canali, E.P. Ambrosio, E. Atzeni, From powders to dense metal parts: characterization of a commercial alsimg alloy processed through direct metal laser sintering, Materials (Basel) 6 (2013) 856–869, https://doi.org/10.3390/ma6030856.
[32] ASTM E10-18, Standard Test Method for Brinell Hardness of Metallic Materials, ASTM Int., 2012 1–36, https://doi.org/10.1520/E0010-15.
[33] K. Kempen, L. Thijs, E. Yasa, M. Badrossamay, W. Verheecke, J.P. Kruth, Process optimization and micostructural analysis for selective laser melting of AlSi10Mg, Solid Free. Fabr. (2011) 484–495.
[34] A. Aversa, M. Lorusso, G. Cattano, D. Manfredi, F. Calignano, E.P. Ambrosio, S. Biamino, P. Fino, M. Lombardi, M. Pavese, A study of the microstructure and the mechanical properties of an AlSiNi alloy produced via selective laser melting, J. Alloys Compd. 695 (2016) 1–9, https://doi.org/10.1016/j.jallcom.2016.10.285.
[35] E.O. Olakanmi, R.F. Cochrane, K.W. Dalgarno, Densification mechanism and microstructural evolution in selective laser sintering of Al-12Si powders, J. Mater. Process. Technol. 211 (2011) 113–121, https://doi.org/10.1016/j.jmatprotec.2010.09.003.
[36] M. Badrossamay, E. Yasa, J. Van Vaerenbergh, J.P. Kruth, Improving Productivity Rate in SLM of Commercial Steel Powders, S. of M. Engineers, Schaumburg, IL, USA, 2009 1–13.